

Control techniques for high-speed dynamic mode imaging in atomic force microscopes

Gayathri Mohan, Chibum Lee and Srinivasa Salapaka

Abstract—This paper proposes a new dynamic mode of operation in an Atomic Force Microscope (AFM) where the deflection signal is used for force regulation instead of its derivatives such as the amplitude and phase. This mode is especially useful in AFMs with high speed positioning systems with bandwidths of the order of $\approx 1/10$ times the natural frequency of the scanning probe. We formulate this problem in an optimal control setting and employ multiobjective optimization techniques to design the regulating controller. Furthermore, we present a method to estimate the tip-sample interaction force and extract the sample topography information from this estimate. The overall scheme facilitates high speed imaging that can potentially exploit fast scanning devices without compromising on the bandwidth and resolution. Simulation results show a regulation bandwidth of 10 – 15% of the natural frequency of the probe.

I. INTRODUCTION

The atomic force microscope is a powerful microcantilever based device that achieves high resolution, nano-scale images of samples and is able to manipulate sample properties at atomic scale [1] (see Figure 1 (a) for the general operation principle). The most common mode of scanning in atomic force microscopy is the tapping mode, where the cantilever is oscillated sinusoidally at or near its resonance frequency (ω_h) using a dither piezo. The amplitude (A) and phase (ϕ) of oscillation change owing to the interatomic forces between the cantilever tip and the sample. In typical tapping mode, the amplitude is regulated to a desired set-point by applying feedback to the z piezo that moves the cantilever up or down to compensate for the features on the sample. This feedback signal forms the image of sample topography.

Amplitude regulation in current AFMs yields good results since the lateral positioning bandwidths are about one percent of resonant frequencies of the cantilevers (1 kHz vs 100 kHz); and therefore the cantilever typically oscillates over many cycles before it experiences appreciable change in sample topography. Therefore, the amplitude, and equivalently the amplitude-regulating control effort provides a reliable measure of the sample topography. However, when the lateral bandwidths are higher, there is appreciable change in the topography even within one or few oscillation cycles. Therefore tapping mode operation cannot harness the advantages of recently emerging high-bandwidth positioning systems,

which provide bandwidths in the order of 10%-20% of the cantilever resonant frequencies [2]–[4].

These advances in positioning bandwidths necessitate high-speed imaging methodologies. Improved bandwidths by separating the goals of force regulation and sample profile estimation, are reported in [5], [6]. In [7], [8] observer-based techniques are applied to sample detection at high speeds and in [9] similar techniques combined with active Q control have been used to image samples with small features. However, since the observer-based methods do not have force regulation, these are unable to measure large changes in the sample topography.

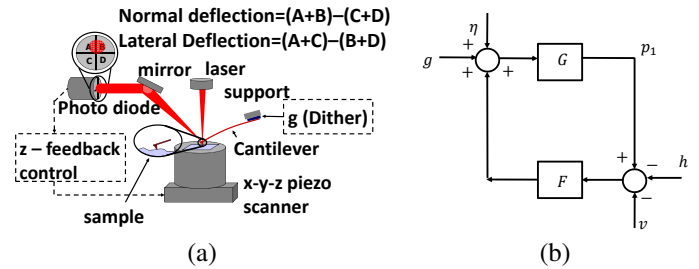


Fig. 1. (a) In a typical AFM, the cantilever is the primary probing device and is excited by the dither input (g). The deflection of the cantilever (p_1) is measured by a laser-mirror arrangement where the change in position of the laser beam is measured by a photo diode sensor. In tapping mode, a common scanning method, the cantilever is oscillated at or near its resonance frequency (ω_h) and the amplitude of oscillation is regulated to a set point using the z -feedback control. (b) G is a model of the cantilever deflection dynamics. It is in loop with the non-linear term $F(p_1 - h - v)$ that represents the interatomic forces between the tip and the sample surface. This forcing term is commonly modeled using the DMT model [10], [11].

In this paper, a model based force regulation technique is developed that uses the ‘fast’ cantilever deflection signal instead of its derivatives such as the oscillation amplitude. The methodology outlined in this paper meets high bandwidth and resolution requirements. Moreover, it achieves imaging speeds of 10 – 15% of the cantilever resonance frequency as compared to current speeds of 0.5 – 3%. The paper is structured as follows: In Section II the primary framework consisting of the original and mock cantilever dynamics along with the error dynamics are presented in state-space form. The objectives that we set out to achieve are defined in terms of closed-loop transfer functions. Section III explains the design of the controller K_1 for regulation in an optimal control setting, K_2 for estimation of the interaction force and the subsequent estimation of sample topography. In Section IV the corresponding simulation results for an example case are presented. Section V and Section VI provide observations, analysis and conclusions based on the results obtained.

Gayathri Mohan, University of Illinois at Urbana-Champaign, IL 61801, USA gmohan2@illinois.edu

Chibum Lee, School of Mechanical Design and Automation Engineering, Seoul National University of Science and Technology, Korea chibum@gmail.com

Srinivasa Salapaka, University of Illinois at Urbana-Champaign, IL 61801, USA salapaka@illinois.edu

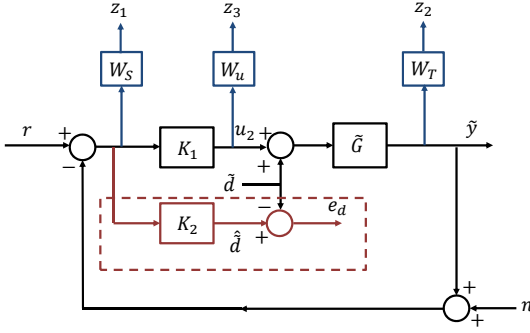


Fig. 2. In this block diagram \tilde{G} represents the error dynamics between the original AFM model (from the dither input to the cantilever output) and the mock system. The controller K_1 is designed to make the dither signal u_2 reject the disturbance \tilde{d} due to the tip-sample interaction forces. Furthermore, K_2 is designed to get an estimate \hat{d} of the disturbance \tilde{d} .

II. OUR FRAMEWORK

Figure 1(a) shows a typical AFM setup and the model for cantilever dynamics is presented in Figure 1(b). For a cantilever of mass m , damping coefficient ζ and resonance frequency ω_n , the deflection dynamics is modeled by,

$$\frac{d^2 \bar{p}}{dt^2} + 2\zeta \omega_n \frac{d\bar{p}}{dt} + \omega_n^2 \bar{p} = u_d + \frac{1}{m} F(\bar{p} - \bar{h} - \bar{v}) + \eta \quad (1)$$

where \bar{p} , \bar{h} and \bar{v} represent the instantaneous cantilever tip position, sample profile and z -actuation signal. The external forces due to dither, interatomic forces between the cantilever tip and the sample, and thermal noise are denoted by u_d , F and η respectively. The dither input u_d is designed as $\omega_n^2 b (\cos(\omega t) + \bar{u}_2(t))$, where b is the amplitude, ω is the oscillation frequency chosen to be near the resonance frequency ω_n and u_2 is the dither input that can be designed to achieve specific objectives, similar to Q-control techniques [7]. The equation is normalized by choosing a new time scale $\tau = \bar{\omega} t$, $p = \frac{\bar{p}}{b}$, $h = \frac{\bar{h}}{b}$, $v = \frac{\bar{v}}{b}$, $\Omega_n = \frac{\omega_n}{\bar{\omega}}$ and $\Omega = \frac{\omega}{\bar{\omega}}$. The scaling constant $\bar{\omega}$ is chosen to be equal or close to the natural frequency of the cantilever. In the redefined co-ordinates, the state-space representation of the AFM model in (1) is written as

$$\begin{aligned} \dot{p} &= Ap + B\Omega_n^2 \cos(\Omega\tau) + Bu_2 + B\frac{1}{m\bar{\omega}^2 b} F(bp_1 - bh - bv) \\ &\quad + B\eta, p(0) = p_0, \\ y &= Cp + n \end{aligned} \quad (2)$$

where $A = \begin{bmatrix} 0 & 1 \\ -\Omega_n^2 & -2\zeta\Omega_n \end{bmatrix}$, $B = \begin{bmatrix} 0 \\ 1 \end{bmatrix}$, $C = \begin{bmatrix} 1 & 0 \end{bmatrix}$, n represents the mechanical noise, and p is the state vector containing the tip position or deflection (p_1) and velocity (p_2). We consider a cantilever subsystem oscillating in air, which we refer to as the mock system,

$$\begin{aligned} \dot{\hat{p}} &= A\hat{p} + B\Omega_n^2 \cos(\Omega\tau) + B\frac{1}{m\bar{\omega}^2 b} F(b\hat{p}_1), \hat{p}(0) = \hat{p}_0 \\ \hat{y} &= C\hat{p}. \end{aligned} \quad (3)$$

The original cantilever subsystem in (2) can be viewed as this mock system augmented with external forces from sample interactions and the additional dither input u_2 . If we denote

$\tilde{p} = p - \hat{p}$ to describe the difference between the real and the mock systems, then its dynamics are given by,

$$\begin{aligned} \dot{\tilde{p}} &= A\tilde{p} + B(u_2 + \tilde{d}), \tilde{p}(0) = p_0 - \hat{p}_0 \\ \tilde{y} &= C\tilde{p} + n, \end{aligned} \quad (4)$$

where the disturbance \tilde{d} represents the tip sample interaction forces, $\frac{1}{m\bar{\omega}^2 b} [F(bp_1 - bh - bv) - F(b\hat{p}_1)]$. The nonlinearities in the p and \hat{p} dynamics that are induced by the interaction force terms are embedded in the external disturbance \tilde{d} in (4). Therefore, the system setup in (4) is viewed as a linear system with a disturbance.

In Figure 2, \tilde{G} represents the error dynamics \tilde{p} . We first pose a regulation problem where controller K_1 is designed to regulate the output $\tilde{y} = p_1 - \hat{p}_1$ to zero. The reference signal r is set to zero. The relevant closed-loop signals required for this design are,

$$\begin{aligned} \tilde{y} &= T(r - n) + \tilde{G}S\tilde{d}, \\ e_m &= S(r - n) - \tilde{G}S\tilde{d}, \\ u_2 &= K_1 S(r - n) - K_1 \tilde{G}S\tilde{d}, \end{aligned} \quad (5)$$

where $e_m = r - \tilde{y} - n$, $S = 1/(1 + \tilde{G}K_1)$ and $T = 1 - S = \tilde{G}K_1/(1 + \tilde{G}K_1)$. The error e_m can be made small by designing S such that S and consequently $\tilde{G}S$ are small in the frequency regions where r , n and \tilde{d} are dominant. The bandwidth ω_{BW} of S characterizes the disturbance rejection bandwidth of the closed-loop system. Designing T to have small roll-off frequency and high roll-off rates ensures high resolution. Robustness to external disturbances is measured by the peak magnitude value of S . Making $\|S\|_\infty$ to be close to 1 improves robustness to modeling uncertainties and disturbances.

III. CONTROLLER DESIGN

A. Disturbance Rejection

The desired objectives are formulated in an optimal control setting based on \mathcal{H}_∞ stacked sensitivity framework [12] (see Figure 2). The objectives of robust stability, disturbance rejection and noise attenuation are realized by shaping the closed-loop transfer functions S and T using weighting functions W_s and W_t . The weighting function W_u imposes boundedness of the control signal u_2 . The weighted error in regulation $z_1 = W_s e_m$, weighted output $z_2 = W_t \tilde{y}$ and weighted dither control signal $z_3 = W_u u_2$ are chosen to be the regulated outputs. The closed-loop transfer function from $w = \begin{bmatrix} \tilde{d} & r - n \end{bmatrix}^T$ to $z = \begin{bmatrix} z_1 & z_2 & z_3 \end{bmatrix}^T$ is given by,

$$\begin{bmatrix} z_1 \\ z_2 \\ z_3 \end{bmatrix} = \underbrace{\begin{bmatrix} -W_s \tilde{G}S & W_s S \\ W_t \tilde{G}S & W_t T \\ -W_u T & W_u K_1 S \end{bmatrix}}_{\Phi} \begin{bmatrix} \tilde{d} \\ r - n \end{bmatrix}. \quad (6)$$

The open-loop system P with external inputs $[w \ u_2]$ and output z is represented as a block diagram in Figure 3. From (6) it is observed that there are a few constraints in the minimization of the closed-loop transfer function (Φ) from w to z . For instance, the fundamental limitation $S + T = I$, conflicts with the simultaneous minimization of terms $W_t \tilde{G}S$ and $W_t T$. This limits the set of feasible controllers

that guarantee small values of $\|\Phi\|_\infty$. However, the sought objectives can be accomplished by selective minimization of certain Φ terms.

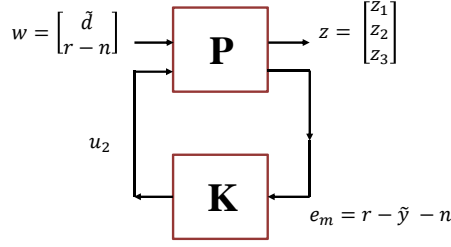


Fig. 3. The generalized framework with plant P and controller K (K_1 in this case). The plant P represents the transfer function from the exogenous inputs w to the regulated variables z . Multiobjective scheme is then employed to realize this alternate optimization problem that minimizes only the transfer functions from w_1 to z_1 and w_2 to z .

We reduce the problem to the minimization of specific transfer functions, $W_s\tilde{G}S$, W_sS , W_tT and W_uK_1S by observing that this minimization achieves closed-loop properties analogous to our desired objectives. Such selective minimization is made possible by the multi-objective scheme proposed in [13]. The term $-W_s\tilde{G}S$ is the transfer function from \tilde{d} to z_1 and $[W_sS \ W_tT \ W_uK_1S]^T$ is the transfer function from $r-n$ to $[z_1 \ z_2 \ z_3]^T$. These constitute the cost functions to be minimized in the multiobjective optimization problem, which is described as,

$$\min_{K_1 \in \mathbf{K}} \gamma \|W_s\tilde{G}S\|_\infty + \left\| \begin{bmatrix} W_sS \\ W_tT \\ W_uK_1S \end{bmatrix} \right\|_\infty \quad (7)$$

where γ can be used to define relative importance between the two cost objectives. The set \mathbf{K} comprises of all the feasible stabilizing controllers K_1 . This multiobjective optimization problem can be cast in terms of linear matrix inequalities (LMIs) [13] (See appendix (a) for a detailed proof). The corresponding LMI conditions for our multi-objective problem can be stated as follows: A solution to the multiobjective optimization problem in (7) exists if there exists a solution $(\hat{A}, \hat{B}, \hat{C}, \hat{D}, R, S, \alpha_1, \alpha_2)$ to the optimization problem,

$$\begin{aligned} & \min \gamma\alpha_1 + \alpha_2 \\ & \text{subject to} \\ & (i) \left[\begin{array}{cccc} \mathcal{Q}(AR + B\hat{C}) & (*) & (*) & (*) \\ \hat{A} + (A + B\hat{D}\hat{C})^T & \mathcal{Q}(SA + \hat{B}\hat{C}) & (*) & (*) \\ (U_1 + B\hat{D}H_1)^T & U_1^T S + H_1^T \hat{B}^T & -\alpha_1 I & (*) \\ V_1 R + E_1 \hat{C} & V_1 + E_1 \hat{D}\hat{C} & D_1 & -\alpha_1 I \end{array} \right] < 0 \\ & (ii) \left[\begin{array}{cccc} \mathcal{Q}(AR + B\hat{C}) & (*) & (*) & (*) \\ \hat{A} + (A + B\hat{D}\hat{C})^T & \mathcal{Q}(SA + \hat{B}\hat{C}) & (*) & (*) \\ (U_2 + B\hat{D}H_2)^T & U_2^T S + H_2^T \hat{B}^T & -\alpha_2 I & (*) \\ V_2 R + E_2 \hat{C} & V_2 + E_2 \hat{D}\hat{C} & D_2 & -\alpha_2 I \end{array} \right] < 0 \\ & (iii) \left[\begin{array}{cc} R & (*) \\ I & S \end{array} \right] > 0. \end{aligned} \quad (8)$$

Here $U_j = B_1 R_j$, $V_j = L_j C_1$, $D_j = L_j D_{11} R_j$, $E_j = L_j D_{12}$ and $H_j = D_{21} R_j$ and the operation $\mathcal{Q}(L) = L + L^T$. The convex optimization problem in (8) is solvable using standard tools

and from its solution, (A_k, B_k, C_k, D_k) can be retrieved since N and M are invertible [14] (see Appendix (b)).

With appropriately designed shaping functions W_s , W_t and W_u , the LMI solution $[A_k, B_k, C_k, D_k]$ gives the most optimal controller K_1 in the feasible set. The shaping functions are constructed carefully to achieve the performance objectives of robust stability, disturbance rejection and noise attenuation. For instance, need for high resolution requires the roll-off frequency of T to be small which is accommodated in the choice of W_t . Similarly, the high bandwidth and robustness aspects require S to be small over a wide range of frequencies and close to 1 values of $\|S\|_\infty$. This is addressed by the choice of W_s (see Section IV).

B. Disturbance Estimation

The next step is to design K_2 (see Figure 2) such that, $\hat{d} = K_2 e_m$ gives an estimate of the tip sample interaction force differential \tilde{d} . In the AFM setup, the deflection p_1 is measurable from sensors, and \hat{p}_1 is also known since it is a state of the mock system. An estimate of \tilde{d} can be numerically obtained from \tilde{y} since,

$$\tilde{y} = p_1 - \hat{p}_1 = \tilde{G}\tilde{d}. \quad (9)$$

Therefore, $S^{-1}\tilde{G}^{-1}\tilde{y}$ is an estimate of \tilde{d} when S is a minimum phase transfer function. However, when the transfer function is non-minimum phase, the Nevanlinna-Pick method can be adopted to design an appropriate inverse transfer function through a minimization problem [15]. Furthermore, we append a stable second-order low-pass filter Ψ , whose cut-off frequency ω_F is larger than the resonance frequency and therefore larger than the highest frequency component of h considered. This guarantees that the transfer function from n to \hat{d} rolls off at high frequencies. Therefore, the controller K_2 is designed as

$$K_2 = -S^{-1}\tilde{G}^{-1}\Psi. \quad (10)$$

Accordingly $\hat{d} = K_2 e_m$ is used as an estimate of \tilde{d} .

As a next step, we present some relations that enable the estimation of the sample topography from the estimate \hat{d} . The nonlinear force of the tip-sample interaction in terms of the separation between the tip and the sample is piecewise continuous and bounded for a practical range of separation distances. On application of mean value theorem to F , the interaction force (from (2) and (3)), results in the following identity,

$$F(bp_1 - bh - bv) - F(b\hat{p}_1) = \Theta(\tau)(b\tilde{p}_1 - bh - bv), \quad (11)$$

where $\Theta = \frac{\partial F}{\partial z}$ with z lying between $(bp_1 - bh - bv)$ and $b\hat{p}_1$. We can assume that the sample topography (h) is approximately a constant over a period of cantilever oscillation and the integral of \tilde{p}_1 is negligible owing to its small values. With these assumptions and $v = 0$ we get,

$$\int_{T-\frac{2\pi}{\omega}}^T [F(bp_1 - bh) - F(b\hat{p}_1)] d\tau = \int_{T-\frac{2\pi}{\omega}}^T \Theta(\tau) d\tau (bh). \quad (12)$$

Therefore, integration of the estimate \hat{d} over every period of cantilever oscillation, facilitates the estimation of the height

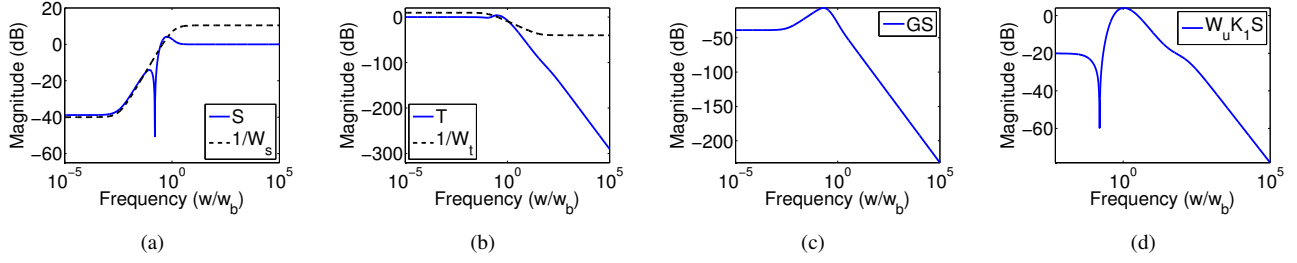


Fig. 4. Minimization problem results are shown using relevant closed-loop transfer functions plotted against the frequencies $\frac{\omega}{\omega_b}$. (a), (b), (c) and (d) show the transfer functions S , T , $\tilde{G}S$ and $W_u K_1 S$ respectively. This optimization yields $\|W_s \tilde{G}S\|_\infty = 1.3745$ and $\left\| \begin{bmatrix} W_s S & W_t T & W_u K_1 S \end{bmatrix}^T \right\|_\infty = 2.5898$

signal $h(\tau)$. It may be noted that the z -piezo actuation signal v can be designed to keep \tilde{d} within the estimation bandwidth of K_2 , but this is not analyzed in this paper.

IV. SIMULATION RESULTS

A. K_1 using LMI approach

The control design formulation described in Section III is applied to a cantilever subsystem with a natural frequency of 69.578kHz and damping $\zeta = 0.0033$. The system equations are normalized as described in Section II with $\tilde{\omega} = \omega_n$ and $b = 2.9155\text{nm}$. Please note that all the plots in this section are made with the normalized parameters, therefore, the y-axis is dimensionless unless specified.

For the design of the controller K_1 , the shaping functions, $W_s = \frac{0.3(s+11.98)}{s+0.03593}$, $W_t = \frac{100(s+1.198)}{s+359.3}$ and $W_u = 0.1$ are chosen to capture the performance objectives of high bandwidth, resolution and robustness to disturbances. As mentioned in

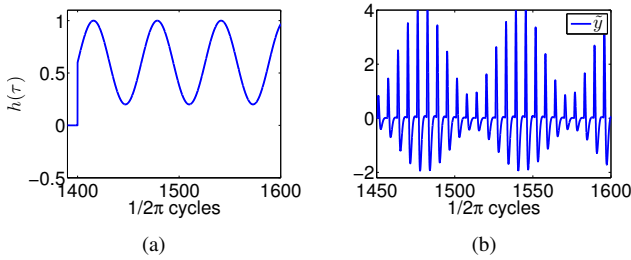


Fig. 5. (a) shows the normalized height profile with frequency $\frac{\omega_h}{\tilde{\omega}} = 0.1$ and amplitude $\frac{a_h}{b} = 0.4$. (b) The regulating action of the controller K_1 makes \tilde{p}_1 settle to zero within a cycle after every tip-sample interaction. These interactions are in the form of impulses, causing instantaneous state jumps of p_1 . It may be noted that in the redefined scales, typical amplitude of p_1 is around 110.

Section II, S should be low for a large range of frequencies where r , \tilde{d} and n are dominant. This and the condition $\|S\|_\infty < 2$ is incorporated in W_s to realize the robustness condition. However, it must be noted that S cannot be made small in frequencies where T is small owing to the fundamental limitation $S + T = I$. The small roll-off frequency and high roll-off rates of T are imposed by W_t . The choice of W_u limits the set of feasible controllers to impose boundedness on the resultant control signal. Employing these weighting functions the generalized transfer function P is constructed. The multiobjective minimization problem in (7) is solved using standard convex optimization tools and the resulting controller is given by $K_1 = \frac{-1191.2589(s-340.3)(s^2+1.075s+0.9207)}{(s+1227)(s+0.0356)(s^2+19.45s+118.9)}$.

The sensitivity function S has a bandwidth ($\approx 15 - 20\%$) of the natural frequency of the cantilever and $\|S\|_\infty = 1.6361$ providing high robustness to modeling uncertainties.

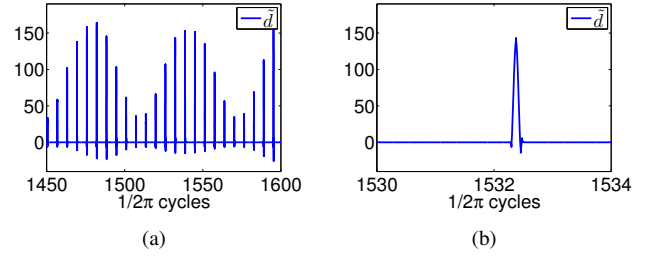


Fig. 6. (a) The forcing from the tip sample interaction occurs as an impulse resulting in instantaneous value change of p_1 and hence \tilde{p} . When the cantilever is within a small distance from the sample, the interaction force impulses occur once every period of oscillation as shown in (b). Note that the x-axis shows $1/2\pi$ cycles.

The simulations implementing K_1 on the \tilde{G} system from (4) were done in Matlab Simulink, for the normalized sinusoidal sample profile shown in Figure 5(a), whose amplitude is a_h/b and frequency is $\omega_h/\tilde{\omega}$. The DMT model was chosen for the tip-sample interaction forcing which has been widely corroborated in literature [10], [11]. The tip sample interaction d occurs in the form of impulses, each time the cantilever interacts with the sample, p_1 assumes a different value instantaneously when this happens (see Figures 6(a), 6(b)). The regulating action brings p_1 to \hat{p}_1 within a cycle as seen in Figure 5(b).

B. Estimation of \tilde{d} with K_2

The disturbance \tilde{d} is estimated directly by passing the \tilde{y} signal in Figure 5(b) through the K_2 controller given by,

$$K_2 = S^{-1} \tilde{G}^{-1} \Psi,$$

where the low pass filter Ψ is chosen to be $\frac{1}{(0.01s+1)^2}$. The magnitude of K_2 obtained is plotted against the normalized frequencies ($\frac{\omega}{\tilde{\omega}}$) in Figure 7(a). The cut-off frequency of the low pass filter Ψ is much higher than the frequency ($\frac{\omega_h}{\tilde{\omega}} = 0.1$) of h , therefore, the estimate retains information about the sample profile. Figures 7(b) and (c) shows \tilde{d} against its estimate $\hat{\tilde{d}} = K_2 \tilde{y}$.

The estimated force difference signal is used to obtain an estimate of the height profile of the sample using the integrator operation described in (12). The state of $\dot{q} =$

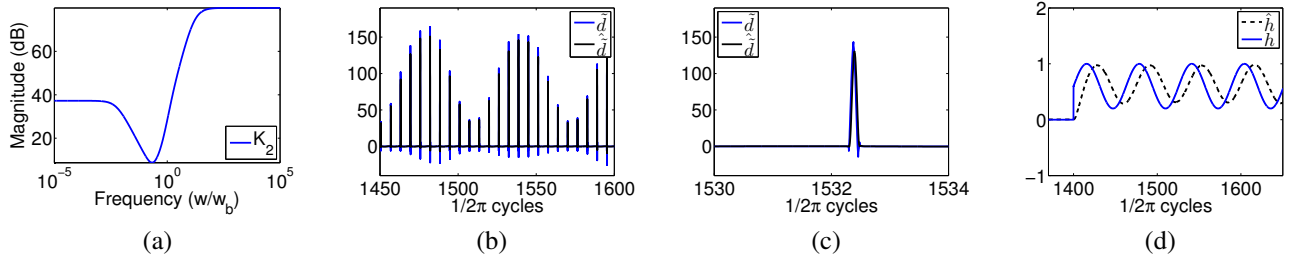


Fig. 7. (a) $K_2 = S^{-1}\tilde{G}^{-1}\Psi$ with $\Psi = \frac{1}{(0.01s+1)^2}$ is used to estimate \tilde{d} from the output \tilde{p}_1 . (b) shows the performance of K_2 as an estimator. (c) shows \tilde{d} and its estimate within a single period of the cantilever oscillation. (d) The estimate \hat{h} is the sample topography estimate obtained by appropriately filtering the integrated values of \hat{d} (13). The estimate is of the same frequency as h , however the estimate does not capture the step function in h causing a phase difference.

$u(T) - u(T - \frac{2\pi}{\omega})$ is equivalent to $\int_{T-\frac{2\pi}{\omega}}^T u(\sigma) d\sigma$. Using this relation, the integral $\int_{T-\frac{2\pi}{\omega}}^T \hat{d}(\sigma) d\sigma$ is computed. From (12) if \hat{d} is a good enough estimate of \tilde{d} , then

$$\int_{T-\frac{2\pi}{\omega}}^T \hat{d}(\tau) d\tau \approx \left(\int_{T-\frac{2\pi}{\omega}}^T \Theta(\tau) d\tau \right) bh. \quad (13)$$

Furthermore, the integrated value of Θ will be a constant over each cycle for the speeds of scanning considered. Consequently, the integrated values of \hat{d} are passed through a second order filter $\frac{1}{(\tau_q s + 1)^2}$. The value of τ_q is chosen be less than $\frac{1}{\omega_h/\omega}$, therefore, the filter retains frequency content of the sample topography, eliminating the high frequency components from p_1 and \hat{p}_1 . The filtered signals have the same frequency and proportional amplitude as h . The factor of proportionality is determined by observing the filtered signals over a few cycles and interpolating the value of the integral of Θ over a cycle. This provides a estimate of the sample topography h (see Figure 7 (d)).

V. ANALYSIS

In this paper, a method for sample topography estimation is presented in Section IV as an example. Since we use a filter of the form $\frac{1}{(\tau_q s + 1)^2}$ in the estimation, the step function in the sample profile is not captured by the estimate \hat{h} and results in a phase difference from the original (see Figure ??). It must be noted that other, possibly more reliable methods, to estimate the sample profile from the disturbance estimate \hat{d} are yet to be explored. For instance, the estimate \hat{d} can be fitted to a force curve model such as the DMT model [10] to get estimates of h .

In this paper, we design the dither input u_2 for force regulation. However, we do not design of the z -actuation signal v . With the knowledge of the estimates \hat{d} and \hat{h} , v design can improve the estimate of \hat{d} further, by keeping \tilde{d} within the estimation bandwidth of the controller.

It has been observed that the interaction force \tilde{d} occurs as impulses or spikes. This is because the cantilever spends only a small fraction of each cycle in contact (i.e. within atomic scale separation) with the sample surface. Therefore, reducing the amplitude of oscillation of the cantilever will increase the its time spent in contact with the sample thereby making the impulse like forcing smoother. Application of low amplitude will make our formulation better suited for sample

property characterization, again using specific models for the interaction force.

In general, derivatives of the deflection signal are used for regulation in the existing dynamic modes because of the low sampling rates (order of 10-100 kHz) of the implementation hardware. Our proposed framework is based on the fast deflection signal with frequencies greater than 100 kHz, demanding much faster sampling rates ($> 3\text{MHz}$). We intend to implement our controller in the experimental AFM setup with the aid of an FPGA based hardware that can satisfy such high sampling rate requirements. Once we implement the controller, we believe that a good characterization of the noises that are present can be obtained. Owing to this we currently omit noise in our simulation results.

VI. CONCLUSION

This paper proposed a method for high-speed imaging in the dynamic mode of the AFM. The primary objective was force regulation using $\tilde{y} = \tilde{p}_1$, which guarantees the regulation of deflection output p_1 to a sinusoidal signal \hat{p}_1 . The force regulation and disturbance estimation problems were separated making the control design procedure two fold. (i) Design of K_1 for the regulation of the the deflection p_1 to a known reference \hat{p} was presented as an LMI based minimization problem with multiple objectives. The regulating controller K_1 is shown to achieve high disturbance rejection bandwidth and good resolution. Especially, since our methodology uses the instantaneous tip position as the sensed signal instead of the slow varying amplitude signal, bandwidth restrictions imposed by demodulation stages are overcome. (ii) The controller K_2 was developed to compute an estimate of the tip-sample interaction forces, which constitute the disturbance in the regulation problem. Moreover, a numerical way to estimate the sample topography from the force estimate is also delineated.

APPENDIX

(a) The generalized plant matrix P (see Figure 3) takes the form,

$$\begin{bmatrix} z_1 \\ z_2 \\ z_3 \\ e_m \end{bmatrix} = \underbrace{\begin{bmatrix} -W_s\tilde{G} & W_s & -W_s\tilde{G} \\ W_t\tilde{G} & 0 & W_t\tilde{G} \\ 0 & 0 & W_u \\ -\tilde{G} & I & -\tilde{G} \end{bmatrix}}_P \begin{bmatrix} \tilde{d} \\ r-n \\ u_2 \end{bmatrix}. \quad (14)$$

The state-space realizations of P and K_1 are written as,

$$\begin{aligned}\dot{x} &= Ax + B_1w + Bu_2, \\ z &= C_1x + D_{11}w + D_{12}u_2,\end{aligned}\quad (15)$$

$$\begin{aligned}e_m &= Cx + D_{21}w \\ \dot{x}_k &= A_kx_k + B_k e_m, \\ u_2 &= C_kx_k + D_k e_m,\end{aligned}\quad (16)$$

with x and x_k being the state vectors of P and K_1 . The overall closed-loop function Φ in terms of this state-space realization can now be computed as,

$$\begin{aligned}\Phi &= \left[\begin{array}{cc|c} A + BD_kC & BC_k & B_1 + BD_kD_{21} \\ B_kC & A_k & B_kD_{21} \\ \hline C_1 + D_{12}D_kC & D_{12}C_k & D_{11} + D_{12}D_kD_{21} \end{array} \right] \\ &=: \left[\begin{array}{c|c} \bar{A} & \bar{B} \\ \hline \bar{C} & \bar{D} \end{array} \right]\end{aligned}\quad (17)$$

We seek an optimal controller of the form (16) that imposes \mathcal{H}_∞ performance on the specific transfer functions $\Phi_1 = W_s\tilde{G}S$ and $\Phi_2 = [W_sS \ W_tT \ W_uK_1S]^T$, which allows us to follow the LMI framework adopted in [13] and [14]. Therefore, we define the following L_j and R_j matrices for $j = 1, 2$,

$$\begin{aligned}L_1 &= \begin{bmatrix} 1 & 0 & 0 \\ 1 & 0 & 0 \\ 0 & 1 & 0 \\ 0 & 0 & 1 \end{bmatrix} & R_1 &= \begin{bmatrix} 1 & 0 \end{bmatrix}^T, \\ L_2 &= \begin{bmatrix} 1 & 0 & 0 \\ 0 & 1 & 0 \\ 0 & 0 & 1 \end{bmatrix} & R_2 &= \begin{bmatrix} 0 & 1 \end{bmatrix}^T.\end{aligned}\quad (18)$$

The choice of the L_j and R_j matrices in (18) are such that, $\Phi_1 = L_1\Phi R_1$ and $\Phi_2 = L_2\Phi R_2$. Let $U_j = B_1R_j$, $V_j = L_jC_1$, $D_j = L_jD_{11}R_j$, $E_j = L_jD_{12}$ and $H_j = D_{21}R_j$. Also, let us denote $\bar{B}R_j$, $L_j\bar{C}$ and $L_j\bar{D}R_j$ by \bar{B}_j , \bar{C}_j and \bar{D}_j respectively. Then each Φ_j for $j = 1, 2$, is

$$\Phi_j = \left[\begin{array}{c|c} \bar{A} & \bar{B}_j \\ \hline \bar{C}_j & \bar{D}_j \end{array} \right].\quad (19)$$

In order to impose the \mathcal{H}_∞ performance objective, we require $\|\Phi_j\|_\infty < \alpha_j$ for $\alpha_j > 0$. This is equivalent to the existence of $P_j > 0$ such that,

$$\begin{bmatrix} \bar{A}^T P_j + P_j \bar{A} & (*) & (*) \\ \bar{B}_j^T P_j & -\alpha_j I & (*) \\ \bar{C}_j & \bar{D}_j & -\alpha_j I \end{bmatrix} < 0,\quad (20)$$

see [16]. However, this is not directly in the LMI form since the terms in (20) are not linear in the variables to be designed, (A_k, B_k, C_k, D_k) . Therefore, we use the following decomposition of the solution P , as shown in [14],

$$P = \begin{bmatrix} S & N \\ N^T & ? \end{bmatrix}, \quad P^{-1} = \begin{bmatrix} R & M^T \\ M^T & ? \end{bmatrix}\quad (21)$$

where ?s denote insignificant terms. Further we define a transformation in terms of the following matrices

$$\Pi_1 = \begin{bmatrix} R & I \\ M^T & 0 \end{bmatrix}, \quad \Pi_2 = \begin{bmatrix} I & S \\ 0 & N^T \end{bmatrix}.\quad (22)$$

The decomposition of P in (21) and the fact that $PP^{-1} = P^{-1}P = I$ implies $MN^T = I - RS$, $\Pi\Pi_1 = \Pi_2$. The redefined variables,

$$\begin{aligned}\hat{A} &= NA_kM^T + NB_kCR + SBC_kM^T \\ &\quad + S(A + BD_kC)R,\end{aligned}\quad (23)$$

$$\hat{B} = NB_k + SBD_k,$$

$$\hat{C} = C_kM^T + D_kCR, \quad \hat{D} = D_k,$$

are used to formulate the optimization problem in terms of LMIs.

(b) From the optimized variables $(\hat{A}, \hat{B}, \hat{C}, \hat{D}, R, S)$, the matrices (A_k, B_k, C_k, D_k) are got as follows:

$$\begin{aligned}A_k &= N^{-1}(\hat{A} - (\hat{B} - S\hat{B}\hat{D})CR - S\hat{B}(\hat{C} - \hat{D}CR) \\ &\quad - S(A + B\hat{D}C)R)M^{-T} \\ B_k &= N^{-1}(\hat{B} - S\hat{B}\hat{D}) \\ C_k &= (\hat{C} - \hat{D}CR)M^{-T} \\ D_k &= \hat{D}\end{aligned}\quad (24)$$

REFERENCES

- [1] G. Binnig, C.F. Quate, and C. Gerber, "Atomic force microscope," *Physical Review Letters*, vol. 56, no. 9, pp. 930–933, March 1986.
- [2] G. Fantner, G. Schitter, and et. al. J.H. Kindt, "Components for high speed atomic force microscopy," *Ultramicroscopy*, vol. 106, no. 8, pp. 881–887, 2006.
- [3] K. Leang and A. Fleming, "High speed afm scanner: Design and drive considerations," in *American Control Conference*, 2008, pp. 3188–3193.
- [4] S. Polit and J. Dong, "Design of high-bandwidth high-precision flexure-based nano-positioning modules," *Journal of Manufacturing Systems*, 2010.
- [5] C. Lee and S. Salapaka, "Fast imaging with alternative signal for dynamic atomic force microscopy," *Applied Physics Letters*, vol. 97, no. 13, 2010.
- [6] S. Salapaka, T. De, and A. Sebastian, "Sample-profile estimate for fast atomic force microscopy," *Applied Physics Letters*, vol. 87, no. 5, 2005.
- [7] D. Sahoo, A. Sebastian, and M. V. Salapaka, "Transient-signal-based sample-detection in atomic force microscopy," *Applied Physics Letters*, vol. 83, no. 26, pp. 5521–5523, December 2003.
- [8] —, "Harnessing the transient signals in atomic force microscopy," *International Journal of Robust and Nonlinear Control*, vol. 15, pp. 805–820, 2005.
- [9] D. Sahoo, P. Agarwal, and M. V. Salapaka, "Transient force atomic force microscopy: A new nano-interrogation method," in *American Control Conference*, 2007, pp. 2136–2140.
- [10] R. Garcia and R. Perez, "Dynamic atomic force microscopy methods," *Surf. Sci. Rep.*, vol. 47, p. 197, 2002.
- [11] R. Garcia and A. S. Paulo, "Attractive and repulsive tip sample interaction regimes in tapping mode atomic force microscopy," *Phys. Rev. B*, vol. 60, no. 7, pp. 4961–4967, August 1999.
- [12] K. Zhou, J. Doyle, and K. Glover, *Robust and Optimal Control*. Prentice Hall, Upper Saddle River, NJ 07458, 1996.
- [13] C. Scherer, P. Gahinet, and M. Chilali, "Multiobjective output-feedback control via lmi optimization," *Automatic Control, IEEE Transactions on*, vol. 42, no. 7, pp. 896–911, July 1997.
- [14] C. Lee and S. Salapaka, "Fast robust nanopositioning - a linear-matrix-inequalities-based optimal control approach," *IEEE/ASME Transactions on Mechatronics*, vol. 14, no. 4, pp. 414–422, August 2009.
- [15] J. Doyle, B. Francis, and A. Tannenbaum, *Feedback Control Theory*. New York: MacMillan, 1992.
- [16] G. Dullerud and F. Paganini, *A Course in Robust Control Theory: A Convex Approach*. Springer-Verlag, 2000.